Article

Data-Driven Investigation of Tellurium-Containing Semiconductors for CO₂ Reduction: Trends in Adsorption and Scaling Relations

Martin Siron, Oxana Andriuc, and Kristin A. Persson*

Cite This: https://doi.org/10.1021/acs.jpcc.2c04810

Read Online

| ACCESS | | Metrics & More | | Article Recommendations | | Supporting Information |

ABSTRACT: Light-assisted conversion of CO₂ into liquid fuels is one of several possible approaches to combating the rise of carbon dioxide emissions. Unfortunately, there are currently no known materials that are efficient, selective, or active enough to facilitate the photocatalytic CO₂ reduction reaction (CO₂RR) at an industrial scale. In this work, we employ density functional theory to explore potential tellurium-containing photocathodes for the CO₂RR by observing trends in adsorption properties arising from over 350 *H, 200 *CO, and 110 *CHO surface−adsorbate structures spanning 39 surfaces of 11 materials. Our results reveal a scaling relationship between *CHO and *H chemisorption energies and charge transfer values, while the scaling relation (typically found in transition metals) between *CO and *CHO adsorption energies is absent. We hypothesize the scaling relation between *H and *CHO to be related to the lone electron located on the bonding carbon atom, while the lack of scaling relation in *CO we attribute to the ability of the lone pair on the C atom to form multiple bonding modes. We compute two predominant orbital-level interactions in the *CO-surface bonds (either using s or p orbitals) in addition to bonding modes involving both σ and π interactions using the Crystal Orbital Hamiltonian Population analysis. We demonstrate that bonds involving the C s orbital are more chemisorptive than the C p orbitals of CO. In general, chemisorption trends demonstrate decreased *H competition with respect to *CO adsorption and enhanced *CHO stability. Finally, we uncover simple element-specific design rules with Te, Se, and Ga sites showing increased competition and Zn, Yb, Rb, Br, and Cl sites showing decreased competition for hydrogen adsorption. We anticipate that these trends will help further screen these materials for potential CO₂RR performance.
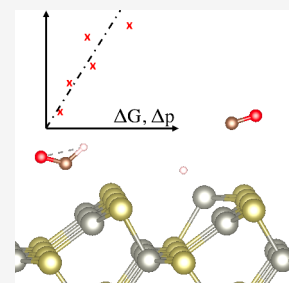
INTRODUCTION

Photocatalytic CO₂ reduction provides a path to reducing greenhouse gas emissions, the accumulation of which is one of the main contributors to climate change.[1−3] Unfortunately, identifying an efficient, stable, and selective heterogeneous photocatalyst with high activity for the CO₂ reduction reaction (CO₂RR) has proven a formidable challenge. Copper is the most widely studied electrocatalyst, known to generate C₂ hydrocarbons with appreciable activity while limiting hydrogen production[4] while, notably, requiring high overpotentials and exhibiting poor stability and selectivity, limiting its practical applications.[5] Compared to electrocatalysts, photocatalysts have the potential advantage of being powered by (sun)light rather than an electric bias. Nevertheless, to date, even the most widely studied materials such as TiO₂ suffer from similar deficiencies as copper: low activity and efficiency.[6] Recently, materials discovery has led to new compositions that have shown dramatic improvements in efficiency and activity, such as W₂C for the photocatalytic and Cu−Al for the electro-catalytic CO₂RR, supporting the need for further materials discovery approaches.[7,8]

In the search for new metallic electrocatalytic materials, significant effort has been made toward calculating chem-isorption energies of adsorbates key to the CO₂RR process, including *CO, *H, and *CHO.[9−11] In many systems (including transition metals,[12] transition metal chalcoge-nides,[13] bimetallics,[14] transition metal oxides[15]), these energies have been linearly correlated to reaction activation energies, according to Brønsted−Evans−Polanyi (BEP) relations.[16−18] For example, CO dissociation energies on transition metal surfaces have been correlated to activity for the CO methanation reaction, where the transition state energy is scaling linearly with the CO dissociation energy.[19] The correlation of chemisorption energies to activity in these material systems has aided in developing design rules for more efficient catalysts. In transition metals, the protonation of CO has been highlighted as the critical step toward CO₂RR products, and its reaction enthalpy has been found to be proportionally related to the overpotential needed to drive the methanation reaction,[20] underscoring the importance to calculating the chemisorption energy of CO, H, and CHO.

In addition to relations between adsorption and activation energies, linear scaling energy relations have also been found between chemisorption energies across various metal and alloy surfaces as a result of similar orbital bonding contributions across these materials: mostly due to the varying contribution from the surface d-orbitals.[21] For such systems, these relations dictate that the adsorption energy of some molecular fragment

A

(i.e., AHx) is linearly correlated with the adsorption energy of a subset of that fragment (i.e., A), such that[21]

$$\Delta E_{AH_x} = \gamma \Delta E_A + \eta \qquad (1)$$

Unfortunately, on transition metals, these scaling relations have been found to limit their activity for the CO_2RR.[22] For example, one key step in the CO_2RR on transition metals is the conversion of *CO to *CHO as an intermediate step to forming value-added products, such as methane. For this to occur, *CHO must be stabilized over *CO. However, because of the scaling relations on metallic materials, a stabilization of *CHO typically indicates a further stabilization of *CO, negatively impacting the CO_2RR process.[22] Hence, there is a need to find materials which can break or improve the scaling relations typically found for transition metal systems and alloys.

In the quest for in-silico discovery of photocatalysts for CO_2RR, Singh et al.[23] conducted a broad search for promising materials without any bias toward a particular class of chemistries. The resulting materials were screened to be synthesizable, stable under CO_2RR aqueous conditions, exhibit theoretical bandgaps in the visible spectrum, and have one or more surface with band-edges at suitable potentials for the CO_2RR.[23] An additional study found that (except for three materials) all of the tellurium-containing semiconductors resulting from the screening strategy had an integrated absorption coefficient near or above that of TiO_2 and that six of the materials considered had small exciton binding energies.[24] In short, on the basis of their stability and photochemical suitability, these tellurium-based materials are promising for the CO_2RR. Additionally, one of the tellurium-containing materials, ZnTe, had recently been experimentally found to exhibit photocatalytic activity,[25−28] giving credibility to the screening. However, semiconducting tellurides have not been investigated for their adsorption properties relevant to the CO_2RR, and further understanding is desirable. To our knowledge, there is no comprehensive database of chemisorption energies or other properties important to photocatalysis that includes data for tellurium-containing materials, and it is uncertain which of these materials may be more optimal for this process.

In this work, we present a comprehensive overview on how *CO, *H, and *CHO interact with various surfaces on materials of interest to the CO_2RR: YbTe, RbTeAu, zinc-blende, wurtzite, and trigonal ZnTe, low-dimensional materials including GaTe, GaTeCl, InTeBr, BiTeBr, as well as Ga_2TeSe_2, and $Zn(GaTe_2)_2$. We present a database of relaxed adsorption structures and chemisorption energies spanning over 350 sites for *H, over 200 sites for *CO and over 110 sites for *CHO, across 39 surfaces of 11 materials—to our knowledge, the most comprehensive set of chemisorption energies (relevant to CO_2 reduction) to date on semiconductors, in this case also focused on those that contain tellurium. Using this database, we uncover the extent of hydrogen adsorption competition in these materials, showing that many surfaces exhibit little to no hydrogen adsorption. Further, we deduce adsorbate−orbital and surface−orbital interactions as they relate to the magnitude of *CO chemisorption energies, where specifically, s-interactions were found to form stronger bonds.

More remarkably, for these tellurium-containing materials with wide differences in chemistries and structures, we uncover a scaling relationship between *H and *CHO. As *H is stabilized on these surfaces, so is *CHO. Meanwhile, we observe a correlation between *CO and *CHO adsorption, but it is not as well-defined as in transition metals. We also observe that *CHO binds more strongly to the surfaces of the studied tellurium materials than to transition metals[29] for the given range of *CO chemisorption energies. Indeed, *CHO chemisorption is much more exergonic, below the scaling relation of transition metals. This suggests more thermodynamically favorable conditions to convert *CO to *CHO on semiconducting tellurides compared to transition metal systems. However, it is unknown if these materials would undergo such a reaction pathway. While further kinetics and mechanistic studies are necessary, this first thermodynamic screening highlights the promising CO_2 reduction activity of tellurium-containing semiconductors and presents a comprehensive overview of trends across this composition landscape which could aid the design of photocatalytic CO_2RR devices.

■ METHODS

The adsorption properties of Te-containing materials were computed using a previously developed adsorption workflow,[30] leveraging the FireWorks,[31] atomate and custodian,[32] and pymatgen[33] python packages. As part of the workflow, density functional theory (DFT) calculations were performed using the Vienna Ab-initio Software Package (VASP)[34,35] using a plane-wave basis set with a typical cutoff energy of 450 eV and projector augmented wave (PAW) pseudopotentials.[36,37] Calculations were performed using the revised PBE functional RPBE,[38] with the Grimme D3 dispersion correction method to account for van der Waals interactions.[39] Dipole corrections were employed for polar slabs. A force-based convergence criterion of 0.05 eV/Å was used, and the self-consistent electronic convergence criterion was set to 1×10^{-4} eV. The k-points density was chosen using the pymatgen default value based on the dimensions of the slab, as described in previous work.[30,33] For all materials, the surfaces under study are from the {100}, {110}, and {111} facet sets. The surfaces were modeled as slabs with a minimum height of 8 Å, minimum length and width of 10 Å, and minimum vacuum size of 20 Å. Adsorption sites were found using the Delauney triangulation method, and for each surface all on-top, bridge, and hollow sites were considered.[30,40] Prior to the geometry optimization of an adsorption structure, four static calculations were performed at the gamma point with the adsorbate placed at different distances from the surface: 0.5, 1.0, 1.5, and 2.0 Å, respectively. The *CO adsorbate was placed vertically on the surface, with the carbon atom nearest to the adsorption site. The *CHO adsorbate was positioned such that the middle carbon atom was affixed on top of the site in consideration. The O and H atom which branch out from the carbon atom were placed pointing away from the surface. The axis connecting the H and O atoms was placed parallel to the "b" direction of the slab. The "a" direction, or any other configuration, including a bidentate configuration, as an input was not tested (a sample *CHO adsorption structure can be found in the Supporting Information). The surface−adsorbate structure corresponding to the lowest energy on the minimal energy landscape obtained from the static calculations was then relaxed. The adsorption energy was calculated from the adsorption structure ground-state energy $E_{ads+slab}$, empty slab ground-state energy E_{slab}, and adsorbate reference energy $E_{adsorbate}$:

$$E_{adsorption} = E_{ads+slab} - E_{slab} - E_{adsorbate} \qquad (2)$$

Table 1. Summary of Material and Surface Properties for Tellurium-Containing Semiconductors

material	lattice	low exciton binding energy[24]	high int abs coefficient[24]	surface {hkl}	cleavage energy (J/m²)
BiTeBr	a, b = 4.4 (4.3[a,48]) c = 6.9 (6.5[a,48]) α, β = 90; γ = 120	√	×	(001)	0.15
Ga₂TeSe₂	a, b = 7.4; c = 11.0 α, β, γ = 90	√	√ (UV)	(101)	0.66
GaTe	a = 18.2 (17.4[a,49]), b = 4.2 (4.1[a,49]), c = 10.8 (10.5[a,49]) α, β = 90, γ = 106 (104[a,49])	√	√ (Vis)	(100)	0.52
GaTeCl	a = 4.2 (4.1[b,50]), b = 5.9 (5.8[b,50]), c = 14.8 (14.3[b,50]) α, β, γ = 90	×	×	(001)	0.12
InTeBr	a, b = 7.7 (7.6[a,51]), c = 8.4 (8.3[a,51]) α, γ = 90, β = 117 (117[a,51])	×	×	(001)	0.11
RbTeAu	a = 5.3 (5.3[b,52]), b = 6.0 (6.0[b,52]), c = 7.4 (7.4[b,52]) α, β, γ = 90	×	×	(001) (010) (100) (101)	0.23 0.67 0.68 0.29
YbTe	a, b, c = 6.4 (6.4[a,53]) α, β, γ = 90	×	√ (UV)	(100) (110)	0.54 0.89
Zn(GaTe₂)₂	a, b = 6.1 (5.9[a,54]) c = 12.0 (12[a,54]) α, β, γ = 90	√	√ (UV–vis)	(100) (101) (110)	5.3 0.55 0.57
ZnTe (mp-2176)	a, b, c = 6.2 (6.1[a,55]) α, β, γ = 90	√	√ (UV)	(110) (111)	0.53 0.92
ZnTe (mp-8884)	a, b = 4.4, c = 7.2 α, β = 90; γ = 120	√	√ (UV)	(100) (110)	0.47 0.48
ZnTe (mp-571195)	a, b = 4.4; c = 10.7 α, β = 90; γ = 120	√	√ (UV)	(100) (101) (110) (111)	0.76 0.82 0.53 0.69

[a]Experimental study. [b]Theoretical study.

Charge transfer analysis was performed using the DDEC6 charge partitioning scheme,[41] where the charge transfer from the slab to the adsorbate was calculated from the charge of the bare slab $\rho_{\text{slab}}^{\text{slab}}$ and the charge of the slab in the adsorption structure $\rho_{\text{slab}}^{\text{slab + ads}}$ using the following formula:

$$\rho_{\text{adsorption}} = \rho_{\text{slab}}^{\text{slab+ads}} - \rho_{\text{slab}}^{\text{slab}} \qquad (3)$$

In addition, a Crystal Orbital Hamiltonian Population (COHP) analysis[42] was performed for the CO and H adsorption structures using the LOBSTER code[43] built into pymatgen.[44] The highest integrated COHP value, up to the Fermi level, for any adsorbate–surface atom pair was selected for further analysis. The adsorbate–surface atom pair was further decomposed into orbital contributions, and the set of orbitals with highest integrated COHP value was recorded.

The DFT binding energies corresponding to the lowest energy (strongest adsorption) structures for each surface and adsorbate were used to investigate any emergent scaling relationships. To convert DFT binding energies into Gibbs free energies of adsorption, the zero-point energy, along with temperature, entropy, and an experimental to theoretical correction term were considered in the following way:

$$\Delta G_{\text{free or ads}} = E_{\text{b}}^{\text{DFT}} + \text{ZPE} + \int c_{\text{p}}\, dT + TS + \mu_{\text{corr}} \qquad (4)$$

The values for the zero-point energy (ZPE), heat constant (c_{p}), entropy contribution (TS) at 292 K, and empirical correction (μ_{corr}) term for the adsorbates under consideration were sourced from the literature[45,46] and can be found in the Supporting Information. The μ_{corr} accounts for the difference between experimental chemical potential and calculated chemical potential of these molecules. The μ_{corr} correction term was only applied to the free molecule and not the adsorbate. In the case of adsorbed CO, the correction is negated by the solvent destabilization, and for H it is negligible.[46] To obtain the electronic energy of free CO, H, and CHO, each molecule was relaxed in a large vacuum cell (20 Å × 20 Å × 20 Å) using the RPBE functional.

The Gibbs free energy of reaction for the formation of CHO (CO + H⁺ + e⁻ → CHO) was computed using the computational hydrogen electrode (CHE) model,[47] which allowed for the calculation of *CHO formation energies through the proton–electron coupled process, using the binding energies of *CHO and *CO on each surface. In this model, the proton–electron chemical potential contribution is assumed to be equal to that of molecular hydrogen $1/2\,\mu(\text{H}_2)$ = $\mu(\text{H}^+ + \text{e}^-)$. Chemical potential corrections for the adsorbed *CHO were obtained from the literature and can be found in the Supporting Information.[47]

RESULTS AND DISCUSSION

Materials and Surfaces. The compounds studied as part of this work are YbTe, RbTeAu, three different phases of ZnTe including zinc-blende, wurtzite, and trigonal, low-dimensional materials including GaTe, GaTeCl, InTeBr, BiTeBr, as well as Ga_2TeSe_2, and $Zn(GaTe_2)_2$. These are 11 of the 17 tellurium-containing materials resulting from the previous computational screening[23] and here prioritized due to their low number of atoms per unit cell and/or low-dimensionality, making them feasible for more advanced computational studies. Because of the novel materials discovery approach of this study, all but ZnTe, YbTe, GaTe, InTeBr, and BiTeBr lacked surface, optoelectronic, or photocatalytic experimental studies, and even more so, two of the materials (RbTeAu and Ga_2TeSe_2) to our knowledge have never been synthesized. While this proved challenging in benchmarking our calculations, we nonetheless performed an exhaustive search of surfaces within the family of {100}, {110}, and {111} facet sets. For much of the analyses, only surfaces with a surface cleavage energy below $1.0 J/m^2$ were considered, omitting only seven surfaces which did not satisfy this criterion.

Three of the compounds considered exhibit a metal−tellurium-halogen composition (M−Te−X). These two-dimensional materials have few unique terminations: for BiTeBr (referenced in the Materials Project[56] as "mp-33723") we considered two nonequivalent surfaces, one bromine and one tellurium-rich, while for both InTeBr ("mp-29236") GaTeCl ("mp-27449"), one single surface was considered due to symmetry (Te−Br-rich for InTeBr and Te-Cl-rich for GaTeCl). Both InTeBr and BiTeBr have been synthesized and their photoluminescence was measured, and we report the computed lattice constants in agreement with experiments within 0.4 Å for the c-axis and 0.1 Å for the other.[48,51] Similarly, in the case of GaTeCl, similar lattice constants were found using higher-order functionals,[50] within 0.5 Å for the c-axis and 0.1 Å for the others. The M−Te−X class of materials showed the lowest cleavage energies of all surfaces considered, in the range of $0.10-0.15 J/m^2$. Detailed lattice constants and surface energies can be found in Table 1. Furthermore, the valence band of the M−Te−X compounds was found to be dominated by tellurium states. In the case of BiTeBr, the conduction band was bismuth-rich, on par with published literature.[57] The conduction band was equally indium- and tellurium-rich for InTeBr, and equally gallium- and tellurium-rich for GaTeCl, consistent with published literature.[58] None of the metal tellurohalogen materials under study present small exciton binding energies, but all have had at least one anisotropic integrated absorption coefficient component above TiO_2.[24]

Another layered material considered in this study, GaTe (referenced in the Materials Project as "mp-542812"), is well studied experimentally for solar cells and optoelectronics, among other applications.[49,59] Because of its layered structure, only the (100) GaTe surface was considered. This surface has equal parts gallium and tellurium species. We overestimated the lattice parameters by 0.8 Å for the a-axis and 0.4 Å for the c-axis, as compared to experimental results.[49] The difference between the calculated and experimentally reported values could potentially be attributed to the epitaxial growth nature of 2D GaTe, or the fact that GGA functionals such as PBE tend to overestimate lattice parameters[60,61] (RPBE included[62]). The (100) surface of GaTe exhibits a cleavage

energy of $0.52 J/m^2$. Our calculated density of states for GaTe shows a predominant tellurium valence band character, with slightly increased gallium character in the conduction band, on par with published literature.[63] Additionally, it has been previously reported that GaTe exhibits a higher absorption coefficient than TiO_2 and a small exciton binding energy.[24]

The consideration of the correct surface is critical when evaluating materials for their photocatalytic CO_2RR capabilities. In the case of YbTe (referenced in the Materials Project as "mp-1779"), a rock-salt structure, it is expected that the nonpolar (100) and the (110) surfaces are experimentally accessible, while the (111) surface is polar and thus energetically unfavorable. Our computed cleavage energies support the expected relative stability of the terminations: 0.54 J/m^2 for the equally Yb−Te-terminating (100) surface, 0.88 J/m^2 for the equally Yb−Te-terminating (110) surface, and 1.82 J/m^2 for the (111) Te-rich surface, one of the highest values reported in our calculations. We emphasize that the stabilization and the possibility to oxygenate, hydroxylate, or hydrogenate these surfaces could change under a reducing aqueous environment.[64] The calculated lattice constant agreed well with experimental studies of bulk YbTe.[53] Unfortunately, YbTe has been reported to exhibit both a large experimental exciton binding energy and a lower absorption coefficient than TiO_2, hindering its use for photocatalytic CO_2RR.[24]

Trigonal ZnTe (referenced in the Materials Project as "mp-571195") is a ZnTe phase that has been reported to exist at high pressure (above 8−9 GPa), thus limiting experimental accessibility.[65] Seven out of 24 surface geometry optimizations successfully converged for trigonal ZnTe: one (100) (equally zinc, tellurium in termination), one (101) (equally zinc, tellurium in termination), three (110) (all tellurium-rich), and two (111) tellurium-rich surfaces. All of the converged surfaces were found to exhibit a cleavage energy below our threshold of $1.0 J/m^2$, with the (110) surfaces being the most stable with a cleavage energy of $0.52 J/m^2$. Two other polymorphs—zincblend and wurtzite—of ZnTe have been experimentally explored under ambient conditions. All seven surfaces in zinc-blende ZnTe (referenced in the Materials Project as "mp-2176") relaxed successfully, and the (110) surface was found to be the most stable with a surface energy of $0.53 J/m^2$, closely followed by the (111) facet. In qualitative agreement, previous experimental work shows exposed (110) surface facets when ZnTe grows in the (111) direction and reports similar surface cleavage energetics.[66] All surfaces considered were equal parts zinc and tellurium in composition. In the case of wurtzite ZnTe (referenced in the Materials Project as "mp-8884"), the geometry optimizations of 10 out of the 16 potential surfaces were successfully completed. Experimentally, wurtzite ZnTe is reported to grow preferentially in the "c" axis direction of its hexagonal crystal system,[67] which indicates that the (001) is highly reactive, e.g., higher energy. Our computed cleavage energies reveal the (100) and (110) surfaces to be the most stable ones ($0.47 J/m^2$ and $0.48 J/m^2$, respectively), while the (001) surface is the least stable one ($1.76 J/m^2$), in qualitative agreement with experimental findings of growth direction preferences. All surfaces considered had an equal zinc and tellurium composition. The similar energetics of the (100) and (110) surfaces, along with the high energy of the (001) termination, could lead to a rod-like Wulff shape and nanowire-like growth, which has been previously reported.[67] Out of the considered ZnTe phases, only cubic ZnTe exhibits a
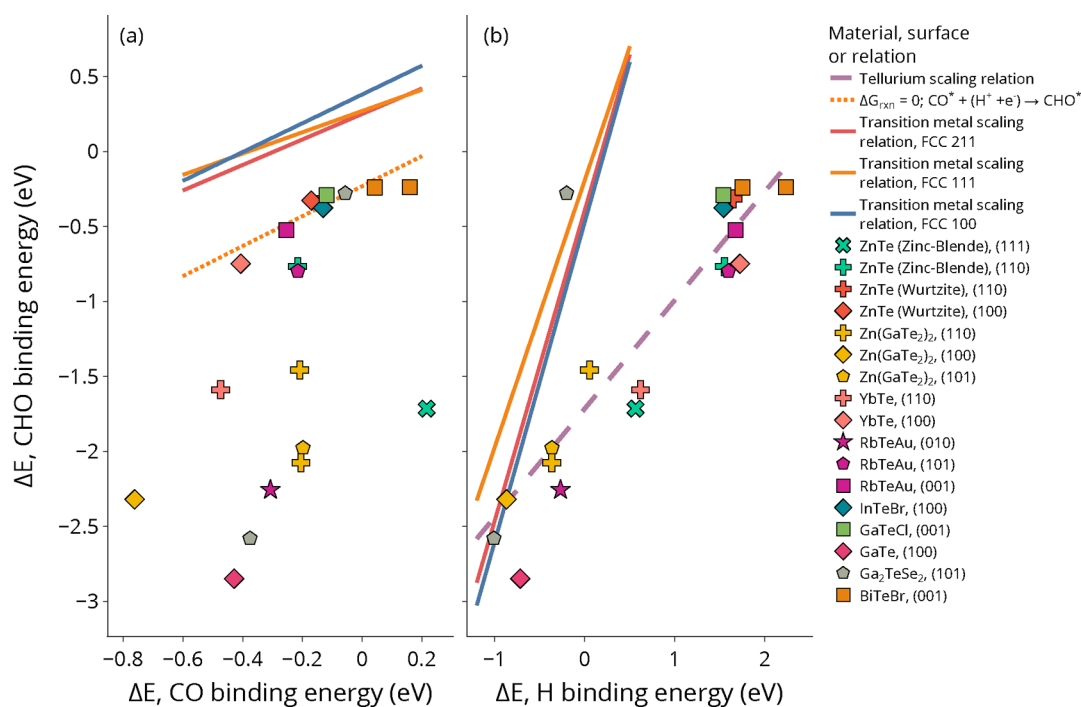
Figure 1. Electronic binding energy of CHO in relation to both (a) CO and (b) H on various tellurium-containing semiconducting surfaces. The minimum energy for each surface is plotted—the optimal site for chemisorption. Transition metal surfaces scaling relations for FCC (100), (111), and (211) are included for comparison.[29] Additionally, a light orange dotted line demarcates where CHO formation is in equilibrium with CO formation, from the CHE model (detailed calculations in Supporting Information). Many materials show increased chemisorption of CHO over CO, especially in comparison to transition metal scaling relationships. A linear relationship can be observed between the H and CHO adsorption energies across the studied tellurium-containing materials (slope of 0.72, an intercept of -1.71, an R^2 value of 0.86, a p-value of 9.07×10^{-6}, and RMSD of 0.44 eV). There is no clear correlation between CO and CHO adsorption energies.

higher absorption coefficient than TiO_2; however, all ZnTe phases exhibit low exciton binding energies.[24]

$Zn(GaTe_2)_2$ (referenced in the Materials Project as "mp-15777") has been predicted computationally to possess promising absorption properties and low exciton binding energies.[24] Our calculations present both a lattice constant and band gap in close agreement to experimental values.[54] Four surfaces fell below the cleavage energy criterion of $1 \, J/m^2$, including the gallium-rich (100), tellurium-rich (101), and two tellurium-rich (110) surfaces with the (101) surface being the most stable one ($0.55 \, J/m^2$), while calculations for 31 surfaces did not converge. A predominant tellurium character is found in $Zn(GaTe_2)_2$ for both the conduction and valence band, consistent with published literature.[68]

To our knowledge, a few of the materials considered here have not yet been experimentally explored or synthesized, including RbTeAu (referenced in the Materials Project as "mp-9008") and Ga_2TeSe_2 (referenced in the Materials Project as "mp-28423"). If these materials can be realized synthetically, we here identify promising surfaces for CO_2 reduction. For example, geometry optimizations of 6 out of 20 possible surfaces in RbTeAu completed successfully: equally rubidium- and tellurium-rich (001), gold-rich (101), equally gold- and tellurium-rich (100), one tellurium-containing and one non-tellurium containing (010) surface, and a high energy equally tellurium- and gold-rich (011) surface (see Table 1). The (001) Te−Rb-terminating surface has previously been studied computationally, including a dynamic stability evaluation[52] and corresponded to our lowest cleavage energy surface of $0.29 \, J/m^2$. In the same theoretical study, the (100) Au−Te terminated surface was also investigated showing no signs of

instability, and the computed cleavage energy for this surface was identified as one of the more stable surfaces.[52] The calculated lattice constants for RbTeAu were found similar to previously reported values.[52] Existing literature reports RbTeAu to exhibit a strong exciton binding energy and poor absorption of visible light, hindering its use for photocatalytic CO_2RR.[24]

The Ga_2TeSe_2 structure has been previously predicted computationally to exhibit a low exciton binding energy.[24] The structure has low symmetry, and only one surface structure, gallium- and tellurium-terminated (101), out of the five that converged successfully, was found here to satisfy the $1 \, J/m^2$ surface energy criterion.

Scaling Relations. To inform design of future photocatalysts, we examined trends in chemisorption energies on tellurium-containing semiconductors between three adsorbate species: *H, *CO, and *CHO. Figure 1a shows the minimum chemisorption energies of *CHO as a function of the minimum chemisorption energies of *CO across each surface and suggests (at best) a weak correlation between surface stabilization of *CHO (more negative chemisorption energy) and *CO adsorption. Breaking down the chemisorption energy site by site rather than surface by surface confirms the absence of a strong scaling relationship between adsorption energies of *CHO and *CO. Given the wide range of composition, chemistries, and structures present in this study, this is not surprising, especially considering that scaling relations in transition metals are partly attributed to the d-orbitals varying contribution.[22] Specifically, in transition metals, strong scaling relationships exist between the adsorption energies of *CO and *CHO for multiple surfaces including the FCC (211),
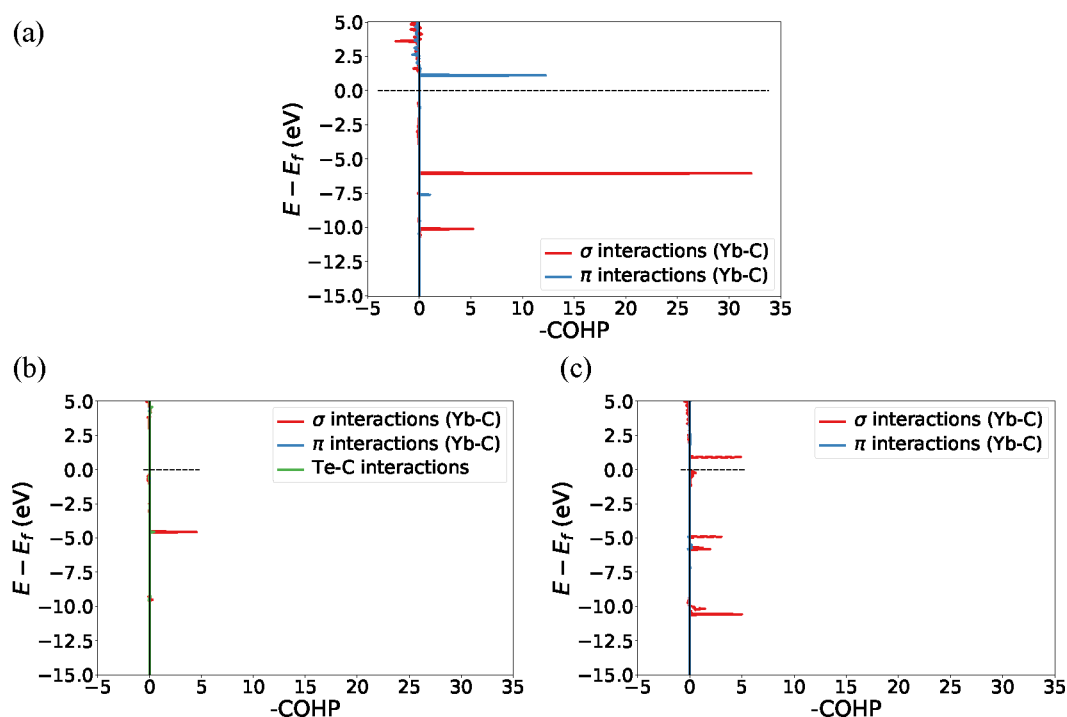
Figure 2. Crystal Orbital Hamiltonian Population Analysis (COHP) between (a) C from CO and nearby Yb atom for CO bonding exhibiting π bonding interactions and having a stronger chemisorptive bond, (b) C from CO and nearby Yb and Te atoms for CO bonding exhibiting no π bonding interactions and having a weaker chemisorptive bond, and (c) C from CHO and nearby Yb atom for an on-top adsorption site. The π interactions result from a summation of the p_x-p_x, p_y-p_y, $d_{x^2-y^2}$ -p_x, $d_{x^2-y^2}$ -p_y, and d_{xz}-p_x interactions and the σ interactions from any s orbital interaction as well as d_{z^2} -p_z, and p_z-p_z interactions. In COHP, the area of the curves are proportional to the number of electrons in the system. All the systems represented above consist of the same number and types of atoms, and thus same number of electrons.

(111), and (100) surfaces.[29] However, in the broad class of semiconducting materials, the role of d-orbitals in the bonding to surface adsorbates is unclear. As shown in Figure 1a, *CHO forms a significantly stronger bond with all the studied telluride surfaces than with any previously investigated transition metals for the observed range of *CO chemisorption energies.[29] Moreover, the chemisorptive strength of *CO falls within a relatively narrow range of values. These observations suggest that if the CO$_2$RR mechanism on tellurides is similar to the ones reported on transition metals, the tellurium-containing materials presented in this study may exhibit lower overpotentials from absorbed CO toward the formation of desirable CO$_2$RR products than transition metals due to their stronger affinity for forming *CHO.[22,69] However, further studies are warranted to confirm the potential mechanistic pathway on these materials.

Applying the CHE model to the reduction of adsorbed *CO to *CHO reveals that many of the studied surfaces exhibit a strong tendency to produce *CHO over *CO, with a few surfaces exhibiting CO hydrogenation exothermic energetics below −1 eV, including two of the RbTeAu (010) surfaces, two of the Zn(GaTe$_2$)$_2$ (100) surfaces, one of the ZnTe (Wurtzite) (110) and ZnTe (zinc-blende) (110) surfaces, Zn(GaTe$_2$)$_2$ (100), and Zn(GaTe$_2$)$_2$ (110). Other surfaces, including the (001) surfaces across all materials, ZnTe (wurtzite) (100), InTeBr (100), YbTe (100), as well as one of the Ga$_2$TeSe$_2$ (101) surfaces straddle the equilibrium Gibbs free energy of the reaction and show limited drive to hydrogenate *CO (dotted yellow line in Figure 1 a). These surfaces show weak inclination to form *CHO over *CO. While transition metal scaling relations dictate a proportional

*CHO to *CO chemisorption, in the tellurium-containing materials considered here, certain surface terminations correlate more or less with the *CHO chemisorptive strength: across these materials, we observe that the (001) surfaces tend to stabilize *CHO and *CO the least (weakest chemisorption energies), followed by the (100) surfaces. The higher index miller planes tend to stabilize *CHO more. The (110) surfaces and the (010) surface of RbTeAu stabilize *CHO the most, which is likely a result of the higher degree of unsaturated bonds in the higher Miller index surface facets.

Remarkably, across all tellurium-containing semiconductors studied in this work, spanning a broad range of structures and chemistries, a strong positive, linear scaling relation was observed between the chemisorption energies of *CHO and *H (Figure 1 b), where surface-stabilized *H correlates strongly with *CHO adsorption. Compared to the scaling relationships reported for transition metals,[29] the one observed for tellurides has a lower slope (0.71 vs 1.7−2.1) and exhibits stronger *CHO chemisorption than on transition metals (except for the Ga$_2$TeSe$_2$ (101) surfaces and the GaTe (100) surface, for which the computed adsorption energies are close to the transition metal relationships). Similarly to what was observed for *CHO and *CO, the adsorption of *H is least stable on the (001) surfaces, followed by the (100) surfaces, while the (101) and (110) surfaces exhibited the lowest/most negative *H adsorption energies.

We hypothesize that the lack of a scaling relationship between *H/*CHO and *CO is due to the ability of *CO to form multiple bonding modes and the similarity in chemistry of *H and *CHO. It is known that *CO can interact with surface species, e.g., by forming both σ and π* backbonding, as
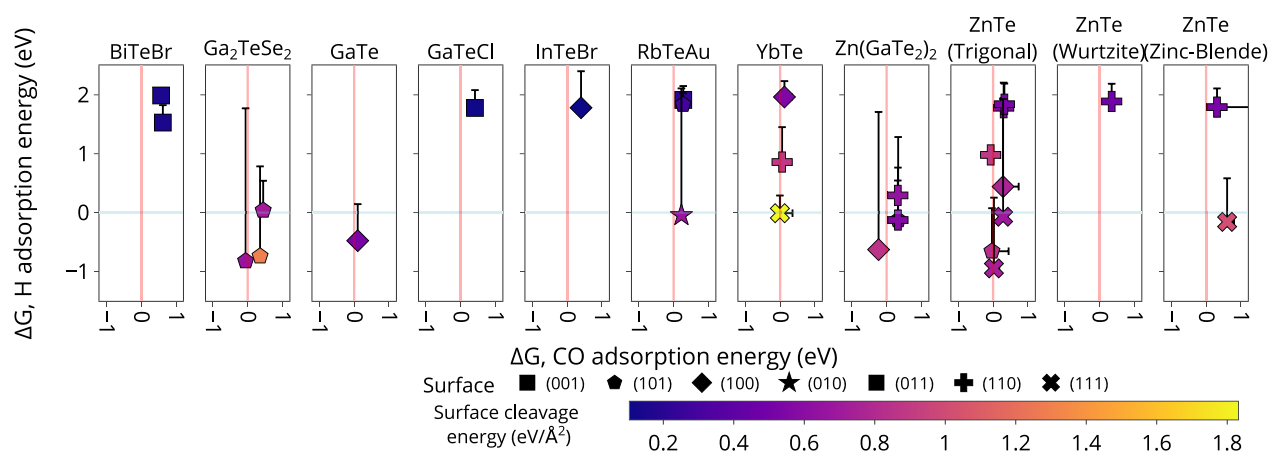
Figure 3. Gibbs free energy of adsorption for CO and H on various surfaces of tellurium-containing semiconductors. Scatter points indicate the minimum of the CO and H adsorption energy on each surface, while error bars indicate the range of adsorption energies on each surface. The points are color-coded by cleavage energy, where purple denotes the most stable surfaces, and yellow denotes the least stable ones. The vertical red line and blue horizontal line indicate the equilibrium Gibbs free energies of adsorption for CO and H, respectively. Most data points are close to, but to the left of, the CO equilibrium line indicating a weak attraction of the corresponding surfaces to CO. A few sites disfavor CO adsorption. While most CO binding energies fall within a narrow range of values (−0.25 to 0.75 eV), H binding energies are spread over a broader range (−1.5 to 2.5 eV). Points above the blue line denote surfaces where *H adsorption is not favored and which might therefore present lower competition from the HER reaction, facilitating the CO₂RR. The points near or below the blue line represent surfaces that are expected to be promising HER catalysts or catalysts poisoned by *H adsorption.

well as by forming more complex bonds. On transition metals, the $\pi*$ backbonding mechanism has been observed, while showing a range of orbital character due to hybridization. Nonetheless, the propensity for backbonding can be attributed to the availability of a partially filled metal d orbital.[70,71] However, the tellurium-containing semiconducting materials studied here exhibit predominantly anionic p-like character. In some materials (such as YbTe), the evidence of a *bimodal* chemisorption energy profile is clear depending on which site the *CO adsorbs to (Yb or Te). YbTe also exhibits a strong d-character projected density of states on its Yb site. As a result, CO positioned close to Yb sites manifests chemisorptive bonds around 1 eV, while *CO positioned near Te show chemisorptive bonds around 0.6 eV. A representative COHP analysis of this behavior is shown in Figure 2a, for a CO positioned near a Yb site of the (100) surface of YbTe, and Figure 2a, for a CO positioned near a Te atom on the (100) surface of YbTe. In this analysis, the *CO bonded to a Yb site exhibits both π- and σ-like bonding character, while the *CO bonded to a Te site only shows σ-bonding character. The fact that some materials can form different and multiple bonding modes with CO may explain why CO does not exhibit a distinct scaling relation with the other adsorbates tested. Meanwhile, *CHO and *H do not exhibit any such element-specific trend on YbTe. In *CHO and *H, the main contribution to bonding originates from the lone electron localized on the C/H atom, respectively. In both cases, we observe predominantly σ-like interactions with the anionic Te- and p-character electrons of the semiconductor surfaces (see Figure 2c) where the on-top Yb site on (100) YbTe for the *CHO adsorbate exhibits little π-bonding interactions, unlike its CO counterpart. For *H, with only a s orbital contributing to bonding, only σ bonds are expected. On-top sites exhibit chemisorptive energies of around −0.5 and 2 eV for *CHO and *H respectively, regardless of the species they adsorb to. Meanwhile, bridge sites exhibit chemisorptive energies of −0.7 and 1.6 eV for *CHO and *H respectively. The positional rather than chemical specificity implies a lack of rearrangement

flexibility of bonding modes in these adsorbates, indicating the participation of similar bonding orbitals and physical overlap.

Furthermore, *CHO and *H exhibit a wide range of DDEC6 charge transfer; meanwhile, *CO exhibits little to no charge transfer activity on these materials—reflecting the higher reactivity of the radical. Further, the increased stabilization (decreased chemisorptive energy) of *CHO and decreased stabilization of *H (increased chemisorptive energy) in comparison to transition metals imply that these materials are likely more carbophobic and oxyphilic;[72] however, further atom probe experiments are warranted. This potentially explains why many *CHO species tend to relax with the O atom tilted toward the surface.

Since the most stable site for *H adsorption is also the most stable site for both *CHO and *CO adsorption on transition metals, scaling relationships limit their ability to drive hydrogenation of *CO. However, while a scaling relationship was observed between *H and *CHO for the studied tellurium materials, the optimal sites for *CO adsorption were typically not the optimal sites for *H or *CHO adsorption. This means that, on these surfaces, even if the *CO binding energy is correlated with the *CHO binding energy, such a scaling relation does not limit the materials' ability to hydrogenate *CO due to the availability of multiple sites. It is important to note that this analysis could only be performed for the surfaces for which the optimization of most adsorption structures converged.

Adsorption Energies. The computed Gibbs free energy of adsorption for *H and *CO is a measure of the thermodynamic drive for these species to bind on the various surfaces and can indicate which of the two adsorbates is more likely to be found on each surface. The computed Gibbs free energy of *H adsorption is positive for many of the surfaces under consideration, including GaTeCl (001), InTeBr (001), both surfaces of BiTeBr (001), RbTeAu (001) (equally rubidium- and tellurium-rich), and (101) (gold-rich), YbTe (100) and (110), ZnTe (trigonal) (100) (equally zinc- and tellurium-rich), Zn(GaTe₂)₂ (110) (tellurium-rich, with zinc

present on surface), and all the (110) surfaces of all ZnTe phases (see Figure 3). On these surfaces, *H adsorption is not expected to compete significantly with *CO adsorption, therefore limiting their *H evolution reaction (HER) capabilities. In contrast, on GaTe (100), Ga_2TeSe_2, the $Zn(GaTe_2)_2$ (100) (gallium-rich) and (101) (tellurium-rich) and one (110) (tellurium-rich but with no zinc on surface), RbTeAu (010), YbTe (111), ZnTe (trigonal) (111) (tellurium-rich) and two zinc-blende (111) (a zinc- and an equally zinc- and tellurium-rich) surfaces and one ZnTe (trigonal) (101) (equally zinc- and tellurium-rich) surface, *H displayed a favorable Gibbs free energy of adsorption (Figure 3). Finally, a few of the analyzed surfaces present similar free energies of adsorption for *H and *CO: Ga_2TeSe_2 (101) (Te-rich) (for which both *H and *CO binding free energies were negative and within 0.03 eV), RbTeAu (010) (equally Rb- and Te-rich), and ZnTe (trigonal) (111) (Te-rich) (Figure 3)). On these surfaces, *H is able to compete with *CO for adsorption, and thus CO_2RR activity may be limited by the HER.

On the basis of the computed values of the Gibbs free energy of adsorption, *CO is weakly repelled on most of the studied surfaces. Surfaces that show Gibbs free energies of adsorption of *CO near or below 0 eV may be more likely to participate in CO reduction if the CO_2RR activity mechanism is similar to that of transition metal systems. Such surfaces include one gallium—tellurium terminated Ga_2TeSe_2 (101) and one gallium-terminated $Zn(GaTe_2)_2$ (100); however, both of these surfaces also indicated strong *H adsorption competition. Some surfaces are much less likely to adsorb *CO, including the other two Ga_2TeSe_2 (101) surfaces (one Te-rich and one equally Te- and Ga-rich), GaTeCl (001), InTeBr (001), all RbTeAu surfaces, two $Zn(GaTe_2)_2$ (110) (both Te-rich) and one $Zn(GaTe_2)_2$ (101) surface (also Te-rich), and all of ZnTe (wurtzite) and ZnTe (zinc-blende) (110) surfaces and two ZnTe (trigonal) surfaces including a (110) Te-rich and (111) also Te-rich surface. Other surfaces, including GaTe (100), all YbTe surfaces, two ZnTe (trigonal) (111) (both Te-rich), two ZnTe (trigonal) (110) (also both Te-rich), and one ZnTe (trigonal) (101) surface (equally Zn- and Te-rich) straddle the equilibrium line for *CO adsorption (Figure 3). These surfaces may not adsorb CO and therefore exhibit a low drive to participate in CO_2RR.

Because of the narrow distribution of *CO chemisorption energies (from −0.25 to 0.75 eV) and the broad distribution of *H chemisorption energies (from −1.0 to 2.5 eV), *H adsorption acts as a key lever to tune selectivity toward either the HER or CO_2RR. In the case of surfaces that are more prone to binding *H over *CO, the adsorption of *H can impede the adsorption and further reduction of *CO. Out of the studied materials, only the ZnTe (trigonal) (111) surface, a Te-rich surface, adsorbs *CO through an exergonic process with a *CO binding energy that is stronger than the H binding energy.

The propensity of low-coordination, undersaturated surface sites to bind adsorbates more strongly than high-coordination atoms has been documented for a variety of systems.[73,74] For H and CHO adsorption, a positive correlation was found between the adsorption energy and increasing coordination number as well as the number of valence electrons of the surface site closest to the adsorbate (see Figure 4). Though not as strongly correlated, an increasing H chemisorption energy was found to correlate with an increase in the number of
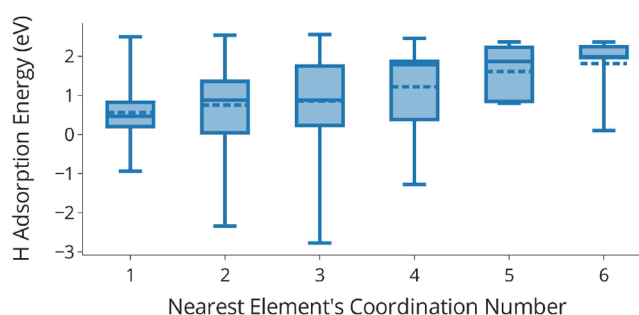

Figure 4. Trends in the coordination number of surface adsorption site and the Gibbs free energy of adsorption for *H.

valence electrons of the surface site closest to the adsorbate. In the case of CHO, a similar trend was observed with respect to the valence of the nearest site neighbor of the C atom adsorption site: as the valence electron number of the nearest site increased, so did the chemisorption energy of CHO and the coordination number. CO adsorption data revealed a similar trend with respect to the valence of the nearest surface atom; however, because of the CO chemisorption energy range being so narrow, this correlation is not as strong. These emerging trends indicate that the chemisorption energies of *H, *CO, and *CHO are influenced by the nature of the element nearest to the adsorbate. When comparing CO and H adsorption for CO_2RR applications, photocatalyst design rules can be compiled by identifying species with a lower tendency toward H adsorption which can therefore aid in preventing HER activity. Typically, for Zn, Yb, Rb, Br, and Cl sites, it was observed that H tends to be less favored than CO for adsorption, indicating that active sites with these elements may limit HER (elemental breakdown figure in Supporting Information). In contrast, Te, Se, and Ga sites showed *H adsorption to be more competitive than CO adsorption, suggesting that these sites could potentially suffer from *H poisoning during the CO_2RR.

Charge Transfer. A charge transfer analysis using the DDEC6 method[41] on over 650 adsorbate-site combinations revealed that very little charge transfer occurs between the adsorbate and the surface, especially for *CO (Figure 5). Most notably, a significant oxidizing charge transfer (near or above $0.1e^-$) of *CO was only observed for a single surface: YbTe (111). This surface also showed a similar propensity to oxidize hydrogen. All other surfaces showed insignificant charge transfer with *CO, typically below $0.05e^-$. The charge transfer values computed for *H adsorption span a broader range than for CO, where many surfaces prefer to form hydride ions upon H adsorption, a reaction shown to be detrimental to the CO_2RR reaction rate in other systems.[75] The hydride forming surfaces include the tellurium-rich surface of BiTeBr (001), GaTe (100), one Ga_2TeSe_2 (101) (tellurium-rich) surface, RbTeAu (101) (gold-rich) and (001) (equally rubidium- and tellurium-rich) surfaces, all $Zn(GaTe_2)_2$ surfaces except for one (110) (tellurium-rich) surface, and most ZnTe surfaces except two, one ZnTe (zinc-blende) (111) (equally zinc- and tellurium-rich), and one ZnTe (zinc-blende) (100) (also equally zinc- and tellurium-rich) surface. Generally, surfaces which tend to form hydride ions also tend to reduce *CHO and vice versa. Within the materials under consideration, YbTe reduces *H and *CHO the most, followed by RbTeAu, then $Zn(GaTe_2)_2$, while Ga_2TeSe_2, InTeBr, and BiTeBr tend to oxidize both species. Surfaces which promoted hydride
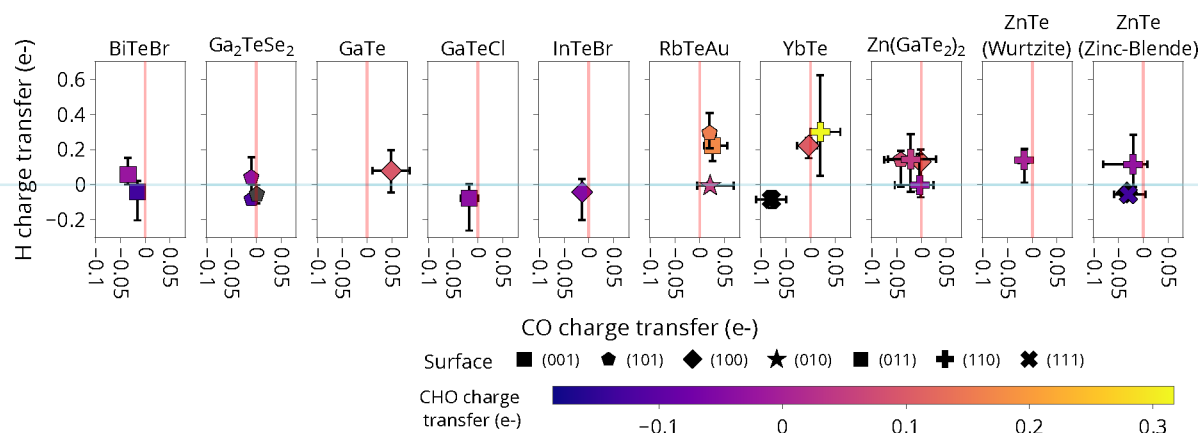
Figure 5. Charge transfer data for CO, H, and CHO adsorbates computed using the DDEC6 method.[41] Positive values indicate a transfer of charge to the adsorbate from the surface, while negative values indicate a transfer of charge from the adsorbate to the surface. The plotted points represent the mean of the charge transfer on all sites for each surface, and the statistical bars indicate the range of charge transfer values across all sites for each surface. The points are color-coded by the mean charge transfer between all sites on that surface and the CHO adsorbate. Data points which are left black and not colored according to *CHO charge transfer colorbar denote less stable surfaces for which *CHO adsorption calculations were not attempted due to their increased computational cost.
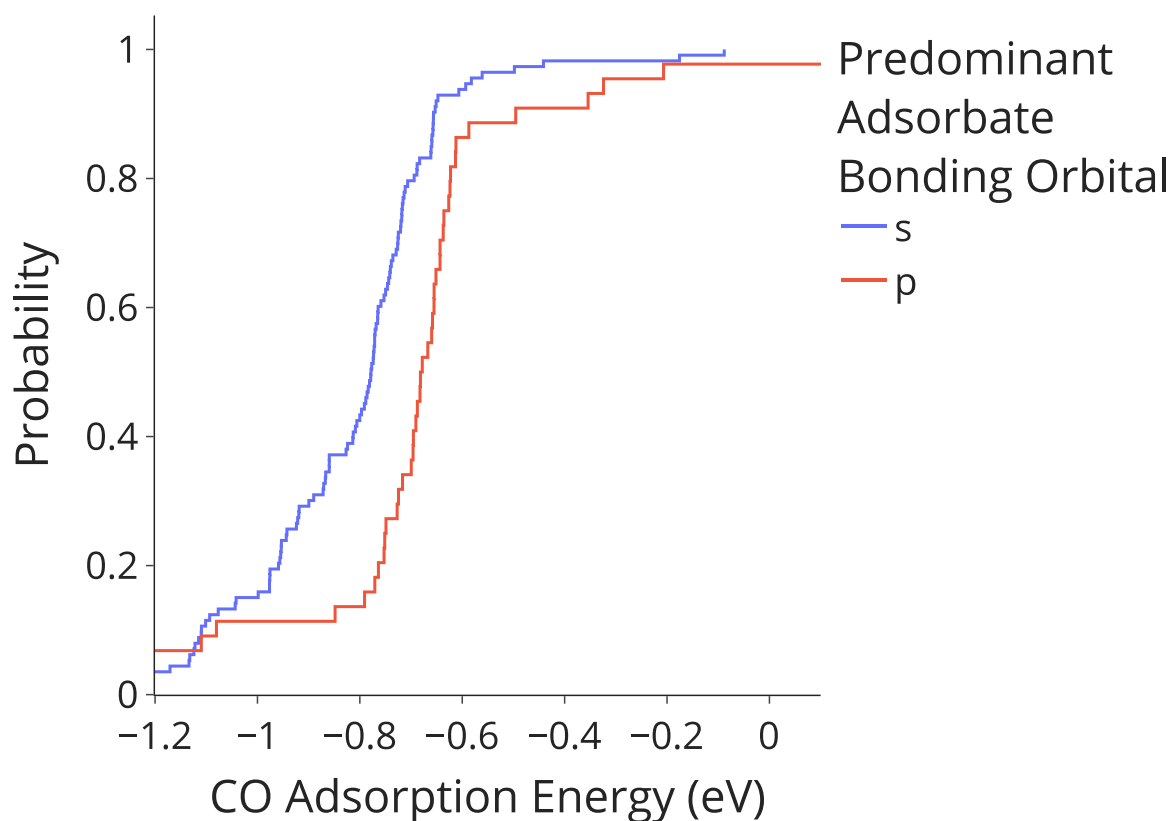

Figure 6. Bonding strength by the predominant carbon orbital in CO as calculated by LOBSTER.[43] When carbon forms a bond with the s orbital, the bond tends to be stronger than when it forms bond with the p-orbital.

formation typically exhibited much larger charge transfer than surfaces which were on the oxidizing side of the charge transfer. In general, it was more likely for *H to be significantly reduced than oxidized, a natural consequence of these materials being chosen for proper band alignment with the CO_2 redox couple, which is typically in alignment with the HER redox couple. The correlation between CHO and H

charge transfer serves as a linear scaling relationship for the tellurium-containing semiconductors considered here (slope of 0.86, intercept of −0.04, R^2 value of 0.88 and p-value of 1.22×10^{-6}). It is interesting to note that the identified scaling relations on these materials for both chemisorption energy and charge transfer are only between H and CHO, but not for CO. This is different from chemisorption scaling relations found on

I

transition metal systems which scales between all adsorbates. While the chemisorption scaling relation had a strong surface dependence, the charge transfer relation was more material-dependent.

Both *CHO and *H charge transfer values showed a strong dependence on the number of valence electrons of the nearest adsorbed site. For both H and CHO, charge transfer into the slab from the adsorbate increased as the valence of the nearest atom increased. This is to be expected, based on the increased stability of closed shells: elements with nearly full valence shells would rather receive charge to achieve a closed shell configuration, while those with near empty valence would rather give charge. The valence dependence implies that the nature of the charge transfer process could potentially be deduced from the nearest element to the adsorbate: both *H and *CHO tend to be reduced by Au, Bi, Rb, Ga, and Yb sites and oxidized by Se, Cl, and Br sites. Our analysis revealed that little charge transfer occurs near Te sites and that Zn sites tend to reduce *H and oxidize *CHO (detailed figure can be found in Supporting Information). Only two of the studied surfaces have the tendency to reduce *CO and oxidize *H: one Ga_2TeSe_2 (101) (equally Ga- and Te-rich) surface and one RbTeAu (010) (equally Rb-, Te-, and Au-rich) surface.

Orbital-Level Contributions. A Crystal Orbital Hamiltonian Population analysis[42] of over 450 relaxed adsorption structures allowed for an orbital-based analysis of the bonding between the surface sites and CO or H. Bonding between the C atom in CO and the surface sites is dominated by the C s or p orbitals, and the p orbital of the surface site. In addition, in the cases where the C s orbital provides the largest contribution to the interaction between CO and the surface, the bonding tends to be much stronger than in the cases in which the main contribution is from the C p orbital (Figure 6). Within the investigated adsorption sites across all materials, very few bonds between the C atom and the surface atom involved a surface d or s orbital. This could partly be explained by the similar electronic structure reported across these materials. As discussed in the Materials and Surfaces section, many of the semiconductors under investigation have a conduction band character dominated by the tellurium species. More specifically, it is typically the tellurium "anion" p orbital which dominates the conduction band character of these chalcogenides, and we therefore expect to observe a strong surface p orbital contribution to the bonds they form with adsorbates. The similarity in bonding contributions and electronic density of states character could also explain the strong scaling relationship observed between CHO and H charge transfer values and chemisorption energies.

CONCLUSIONS

In this work, we present a comprehensive set of surface–adsorbate calculations for tellurium-containing semiconductors, containing over 650 calculations across 39 surfaces of 11 materials. The analysis of this data set reveled two important scaling relationships: between the CHO and H chemisorption energies, as well as between their charge transfer properties. The charge transfer scaling relationship identified is, to our knowledge, a novel relationship for semiconductor adsorption. The scaling relations between *CHO and *H could significantly lower the cost of future computational work and serve as a descriptor for *CHO adsorption. Additionally, we hypothesize that the scaling relation behind *CHO and *H originates from the lone electron on the H and C atom, while

*CO exhibits multiple bonding modes which breaks the relationship. We compared the calculated chemisorption energies and scaling relationships to what has been previously reported for transition metals, and the observed differences between these two classes of materials suggest that tellurium semiconductors have the potential to exhibit enhanced CO_2RR capabilities compared to their counterparts. We identified surfaces with both high and low *H adsorption competition and investigated the orbital contributions to the bonding between the surface and adsorbates, and found that in general in many surfaces, *H adsorption is not as competitive as *CO adsorption; however, many surfaces are not thermodynamically inclined to adsorb *CO. Meanwhile, *CHO is found to stabilize on these surfaces. The computed Gibbs free energies of adsorption could serve as a guide for investigating the propensity of the studied surfaces to facilitate CO_2RR; however, further mechanistic studies are needed to allow for a definite assessment of CO_2RR capabilities. Finally, we provide a series of element-specific design rules for improved charge transfer and chemisorption properties for the CO_2RR to aid in the design of selective and efficient photocatalysts.

■ ASSOCIATED CONTENT

■ AUTHOR INFORMATION

Corresponding Author

Kristin A. Persson − *Department of Materials Science and Engineering, University of California, Berkeley, California 94720, United States; Molecular Foundry, Lawrence Berkeley National Laboratory, Berkeley, California 94720, United States;* ⓞ orcid.org/0000-0003-2495-5509; Email: kapersson@lbl.gov

Authors

Martin Siron − *Department of Materials Science and Engineering, University of California, Berkeley, California 94720, United States; Liquid Sunlight Alliance, Lawrence Berkeley National Laboratory, Berkeley, California 94720, United States;* ⓞ orcid.org/0000-0002-4562-7814

Oxana Andriuc − *Department of Chemistry, University of California, Berkeley, California 94720, United States; Liquid Sunlight Alliance, Lawrence Berkeley National Laboratory, Berkeley, California 94720, United States;* ⓞ orcid.org/0000-0002-4011-3339

Complete contact information is available at:
https://pubs.acs.org/10.1021/acs.jpcc.2c04810

Notes

The authors declare no competing financial interest.

■ ACKNOWLEDGMENTS

■ REFERENCES

(1) Khatib, H. IEA World Energy Outlook 2011—A comment. *Energy Policy* **2012**, *48*, 737−743. Special Section: Frontiers of Sustainability

(2) *Fifth Assessment Report of the Intergovernmental Panel on Climate Change*; Intergovernmental Panel on Climate Change (IPCC), United Nations, 2014.

(3) Gust, D.; Moore, T. A.; Moore, A. L. Solar Fuels via Artificial Photosynthesis. *Acc. Chem. Res.* **2009**, *42*, 1890−1898.

(4) Hori, Y. In *Modern Aspects of Electrochemistry*; Vayenas, C. G., White, R. E., Gamboa-Aldeco, M. E., Eds.; Springer New York: New York, NY, 2008; pp 89−189.

(5) Ye, W.; Guo, X.; Ma, T. A review on electrochemical synthesized copper-based catalysts for electrochemical reduction of CO2 to C2+ products. *Chemical Engineering Journal* **2021**, *414*, 128825.

(6) Wu, J.; Huang, Y.; Ye, W.; Li, Y. CO2 Reduction: From the Electrochemical to Photochemical Approach. *Advanced Science* **2017**, *4*, 1700194.

(7) Esmaeilirad, M.; Baskin, A.; Kondori, A.; Sanz-Matias, A.; Qian, J.; Song, B.; Tamadoni Saray, M.; Kucuk, K.; Belmonte, A. R.; Delgado, P. N. M.; Park, J.; Azari, R.; Segre, C. U.; Shahbazian-Yassar, R.; Prendergast, D.; Asadi, M. Gold-like activity copper-like selectivity of heteroatomic transition metal carbides for electrocatalytic carbon dioxide reduction reaction. *Nat. Commun.* **2021**, *12*, 5067.

(8) Zhong, M.; Tran, K.; Min, Y.; Wang, C.; Wang, Z.; Dinh, C.-T.; De Luna, P.; Yu, Z.; Rasouli, A. S.; Brodersen, P.; et al. Accelerated discovery of CO2 electrocatalysts using active machine learning. *Nature* **2020**, *581*, 178−183.

(9) Ma, Z.; Zaera, F. Organic chemistry on solid surfaces. *Surf. Sci. Rep.* **2006**, *61*, 229−281.

(10) Nørskov, J. K.; Bligaard, T.; Rossmeisl, J.; Christensen, C. H. Towards the computational design of solid catalysts. *Nat. Chem.* **2009**, *1*, 37−46.

(11) Nørskov, J. K.; Studt, F.; Abild-Pedersen, F.; Bligaard, T. *Fundamental Concepts in Heterogeneous Catalysis*; John Wiley & Sons, 2014.

(12) Peterson, A. A.; Nørskov, J. K. Activity Descriptors for CO2 Electroreduction to Methane on Transition-Metal Catalysts. *J. Phys. Chem. Lett.* **2012**, *3*, 251−258.

(13) Ji, Y.; Nørskov, J. K.; Chan, K. Scaling Relations on Basal Plane Vacancies of Transition Metal Dichalcogenides for CO2 Reduction. *J. Phys. Chem. C* **2019**, *123*, 4256−4261.

(14) Ko, J.; Kwon, H.; Kang, H.; Kim, B.-K.; Han, J. W. Universality in surface mixing rule of adsorption strength for small adsorbates on binary transition metal alloys. *Phys. Chem. Chem. Phys.* **2015**, *17*, 3123−3130.

(15) Tayyebi, E.; Hussain, J.; Abghoui, Y.; Skúlason, E. Trends of Electrochemical CO2 Reduction Reaction on Transition Metal Oxide Catalysts. *J. Phys. Chem. C* **2018**, *122*, 10078−10087.

(16) Bligaard, T.; Nørskov, J.; Dahl, S.; Matthiesen, J.; Christensen, C.; Sehested, J. The Brønsted−Evans−Polanyi relation and the volcano curve in heterogeneous catalysis. *J. Catal.* **2004**, *224*, 206−217.

(17) Evans, M. G.; Polanyi, M. Inertia and driving force of chemical reactions. *Trans. Faraday Soc.* **1938**, *34*, 11−24.

(18) Bronsted, J. N. Acid and Basic Catalysis. *Chem. Rev.* **1928**, *5*, 231−338.

(19) Bligaard, T.; Nørskov, J.; Dahl, S.; Matthiesen, J.; Christensen, C.; Sehested, J. The Brønsted−Evans−Polanyi relation and the volcano curve in heterogeneous catalysis. *J. Catal.* **2004**, *224*, 206−217.

(20) Peterson, A. A.; Nørskov, J. K. Activity Descriptors for CO2 Electroreduction to Methane on Transition-Metal Catalysts. *J. Phys. Chem. Lett.* **2012**, *3*, 251−258.

(21) Abild-Pedersen, F.; Greeley, J.; Studt, F.; Rossmeisl, J.; Munter, T. R.; Moses, P. G.; Skúlason, E.; Bligaard, T.; Nørskov, J. K. Scaling Properties of Adsorption Energies for Hydrogen-Containing Molecules on Transition-Metal Surfaces. *Phys. Rev. Lett.* **2007**, *99*, 016105.

(22) Li, Y.; Sun, Q. Recent Advances in Breaking Scaling Relations for Effective Electrochemical Conversion of CO2. *Adv. Energy Mater.* **2016**, *6*, 1600463.

(23) Singh, A. K.; Montoya, J. H.; Gregoire, J. M.; Persson, K. A. Robust and Synthesizable Photocatalysts for CO2 Reduction: A Data-driven Materials Discovery. *Nat. Commun.* **2019**, *10*, 443.

(24) Biswas, T.; Singh, A. K. Excitonic effects in absorption spectra of carbon dioxide reduction photocatalysts. *npj Comput. Mater.* **2021**, *7*, 189.

(25) Ehsan, M. F.; Ashiq, M. N.; Bi, F.; Bi, Y.; Palanisamy, S.; He, T. Preparation and Characterization of SrTiO3−ZnTe Nanocomposites for the Visible-light Photoconversion of Carbon Dioxide to Methane. *RSC Adv.* **2014**, *4*, 48411−48418.

(26) Ehsan, M. F.; He, T. In Situ Synthesis of ZnO/ZnTe Common Cation Heterostructure and Its Visible-light Photocatalytic Reduction of CO2 into CH4. *Appl. Catal., B* **2015**, *166−167*, 345−352.

(27) Jang, Y. J.; Lee, J.; Lee, J.; Lee, J. S. Solar Hydrogen Production from Zinc Telluride Photocathode Modified with Carbon and Molybdenum Sulfide. *ACS Appl. Mater. Interfaces* **2016**, *8*, 7748−7755.

(28) Jang, Y. J.; Jeong, I.; Lee, J.; Lee, J.; Ko, M. J.; Lee, J. S. Unbiased Sunlight-Driven Artificial Photosynthesis of Carbon Monoxide from CO2 Using a ZnTe-Based Photocathode and a Perovskite Solar Cell in Tandem. *ACS Nano* **2016**, *10*, 6980−6987.

(29) Shi, C.; Hansen, H. A.; Lausche, A. C.; Nørskov, J. K. Trends in electrochemical CO2 reduction activity for open and close-packed metal surfaces. *Phys. Chem. Chem. Phys.* **2014**, *16*, 4720−4727.

(30) Andriuc, O.; Siron, M.; Montoya, J. H.; Horton, M.; Persson, K. A. Automated Adsorption Workflow for Semiconductor Surfaces and the Application to Zinc Telluride. *J. Chem. Inf. Model.* **2021**, *61*, 3908−3916.

(31) Jain, A.; Ong, S. P.; Chen, W.; Medasani, B.; Qu, X.; Kocher, M.; Brafman, M.; Petretto, G.; Rignanese, G.-M.; Hautier, G.; et al. Fireworks: A Dynamic Workflow System Designed for High-throughput Applications: Fireworks: A Dynamic Workflow System Designed for High-Throughput Applications. *Concurrency Computat.: Pract. Exp.* **2015**, *27*, 5037−5059.

(32) Mathew, K.; Montoya, J. H.; Faghaninia, A.; Dwarakanath, S.; Aykol, M.; Tang, H.; Chu, I.-h.; Smidt, T.; Bocklund, B.; Horton, M.; et al. Atomate: A High-level Interface to Generate, Execute, and Analyze Computational Materials Science Workflows. *Comput. Mater. Sci.* **2017**, *139*, 140−152.

(33) Ong, S. P.; Richards, W. D.; Jain, A.; Hautier, G.; Kocher, M.; Cholia, S.; Gunter, D.; Chevrier, V. L.; Persson, K. A.; Ceder, G. Python Materials Genomics (pymatgen): A Robust, Open-source Python Library for Materials Analysis. *Comput. Mater. Sci.* **2013**, *68*, 314−319.

(34) Kresse, G.; Furthmüller, J. Efficiency of Ab-initio Total Energy Calculations for Metals and Semiconductors Using a Plane-wave Basis Set. *Comput. Mater. Sci.* **1996**, *6*, 15−50.

(35) Kresse, G.; Furthmüller, J. Efficient Iterative Schemes for *Ab Initio* Total-energy Calculations Using a Plane-wave Basis Set. *Phys. Rev. B* **1996**, *54*, 11169−11186.

(36) Blöchl, P. E. Projector Augmented-wave Method. *Phys. Rev. B* **1994**, *50*, 17953−17979.

(37) Kresse, G.; Joubert, D. From Ultrasoft Pseudopotentials to the Projector Augmented-wave Method. *Phys. Rev. B* **1999**, *59*, 1758−1775.

(38) Hammer, B.; Hansen, L. B.; Nørskov, J. K. Improved Adsorption Energetics Within Density-functional Theory Using Revised Perdew-Burke-Ernzerhof Functionals. *Phys. Rev. B* **1999**, *59*, 7413−7421.

(39) Grimme, S.; Antony, J.; Ehrlich, S.; Krieg, H. A Consistent and Accurate *ab initio* Parametrization of Density Functional Dispersion Correction (DFT-D) for the 94 Elements H-Pu. *J. Chem. Phys.* **2010**, *132*, 154104.

(40) Montoya, J. H.; Persson, K. A. A high-throughput framework for determining adsorption energies on solid surfaces. *npj Comput. Mater.* **2017**, *3*, 14.

(41) Manz, T. A.; Limas, N. G. Introducing DDEC6 Atomic Population Analysis: Part 1. Charge Partitioning Theory and Methodology. *RSC Adv.* **2016**, *6*, 47771−47801.

(42) Dronskowski, R.; Bloechl, P. E. Crystal orbital Hamilton populations (COHP): energy-resolved visualization of chemical bonding in solids based on density-functional calculations. *J. Phys. Chem.* **1993**, *97*, 8617−8624.

(43) Maintz, S.; Deringer, V. L.; Tchougréeff, A. L.; Dronskowski, R. LOBSTER: A tool to extract chemical bonding from plane-wave based DFT. *J. Comput. Chem.* **2016**, *37*, 1030−1035.

(44) Nelson, R.; Ertural, C.; George, J.; Deringer, V. L.; Hautier, G.; Dronskowski, R. LOBSTER: Local orbital projections, atomic charges, and chemical-bonding analysis from projector-augmented-wave-based density-functional theory. *J. Comput. Chem.* **2020**, *41*, 1931−1940.

(45) Studt, F.; Abild-Pedersen, F.; Varley, J. B.; Nørskov, J. K. CO and CO2 Hydrogenation to Methanol Calculated Using the BEEF-vdW Functional. *Catal. Lett.* **2013**, *143*, 71−73.

(46) Tran, K.; Ulissi, Z. W. Active learning across intermetallics to guide discovery of electrocatalysts for CO2 reduction and H2 evolution. *Nature Catalysis* **2018**, *1*, 696−703.

(47) Peterson, A. A.; Abild-Pedersen, F.; Studt, F.; Rossmeisl, J.; Nørskov, J. K. How copper catalyzes the electroreduction of carbon dioxide into hydrocarbon fuels. *Energy Environ. Sci.* **2010**, *3*, 1311−1315.

(48) Sans, J. A.; Manjón, F. J.; Pereira, A. L. J.; Vilaplana, R.; Gomis, O.; Segura, A.; Muñoz, A.; Rodríguez-Hernández, P.; Popescu, C.; Drasar, C.; et al. Structural, vibrational, and electrical study of compressed BiTeBr. *Phys. Rev. B* **2016**, *93*, 024110.

(49) Borisenko, E.; Borisenko, D.; Timonina, A.; Kolesnikov, N. Nonvariant polymorphic transition from hexagonal to monoclinic lattice in GaTe single crystal. *J. Cryst. Growth* **2020**, *535*, 125548.

(50) Zhang, S.-H.; Liu, B.-G. A controllable robust multiferroic GaTeCl monolayer with colossal 2D ferroelectricity and desirable multifunctionality. **2018**, *10*, 5990−5996.

(51) Kniep, R.; Wilms, A. Phase relations in the InBr3 - In2Te3 system and the crystal structure of InTeBr. *Mater. Res. Bull.* **1980**, *15*, 763−770.

(52) Liu, Q.-B.; Wang, Z.-Q.; Fu, H.-H. Ideal topological nodal-surface phonons in RbTeAu-family materials. *Phys. Rev. B* **2021**, *104*, L041405.

(53) Kaldis, E.; Peteler, W. High temperature evaporation of YbTe: Thermodynamics, mass spectrometry and surface analysis. *J. Cryst. Growth* **1981**, *52*, 125−130.

(54) Mayengbam, R.; Tripathy, S.; Palai, G.; Dhar, S. First-principles study of phase transition, electronic, elastic and optical properties of

defect chalcopyrite ZnGa2Te4 semiconductor under different pressures. *J. Phys. Chem. Solids* **2018**, *119*, 193−201.

(55) Mahalingam, T.; John, V.; Rajendran, S.; Sebastian, P. Electrochemical deposition of ZnTe thin films. *Semiconductor science and technology* **2002**, *17*, 465.

(56) Jain, A.; Ong, S. P.; Hautier, G.; Chen, W.; Richards, W. D.; Dacek, S.; Cholia, S.; Gunter, D.; Skinner, D.; Ceder, G.; et al. Commentary: The Materials Project: A materials genome approach to accelerating materials innovation. *APL Materials* **2013**, *1*, 011002.

(57) Schwalbe, S.; Wirnata, R.; Starke, R.; Schober, G. A. H.; Kortus, J. Ab initio electronic structure and optical conductivity of bismuth tellurohalides. *Phys. Rev. B* **2016**, *94*, 205130.

(58) Zhang, S.-H.; Liu, B.-G. A controllable robust multiferroic GaTeCl monolayer with colossal 2D ferroelectricity and desirable multifunctionality. *Nanoscale* **2018**, *10*, 5990−5996.

(59) Cui, Y.; Caudel, D. D.; Bhattacharya, P.; Burger, A.; Mandal, K. C.; Johnstone, D.; Payne, S. A. Deep levels in GaTe and GaTe:In crystals investigated by deep-level transient spectroscopy and photoluminescence. *J. Appl. Phys.* **2009**, *105*, 053709.

(60) Zhang, G.-X.; Reilly, A. M.; Tkatchenko, A.; Scheffler, M. Performance of various density-functional approximations for cohesive properties of 64 bulk solids. *New J. Phys.* **2018**, *20*, 063020.

(61) Haas, P.; Tran, F.; Blaha, P. Calculation of the lattice constant of solids with semilocal functionals. *Phys. Rev. B* **2009**, *79*, 085104.

(62) Smeets, E. W. F.; Voss, J.; Kroes, G.-J. Specific Reaction Parameter Density Functional Based on the Meta-Generalized Gradient Approximation: Application to H2 + Cu(111) and H2 + Ag(111). *J. Phys. Chem. A* **2019**, *123*, 5395−5406.

(63) Sánchez-Royo, J. F.; Pellicer-Porres, J.; Segura, A.; Muñoz Sanjosé, V.; Tobías, G.; Ordejón, P.; Canadell, E.; Huttel, Y. Angle-resolved photoemission study and first-principles calculation of the electronic structure of GaTe. *Phys. Rev. B* **2002**, *65*, 115201.

(64) Wander, A.; Bush, I. J.; Harrison, N. M. Stability of rocksalt polar surfaces: An ab initio study of MgO(111) and NiO(111). *Phys. Rev. B* **2003**, *68*, 233405.

(65) Ovsyannikov, S. V.; Shchennikov, V. V. Phase transitions investigation in ZnTe by thermoelectric power measurements at high pressure. *Solid State Commun.* **2004**, *132*, 333−336.

(66) Sun, Y.; Zhao, Q.; Gao, J.; Ye, Y.; Wang, W.; Zhu, R.; Xu, J.; Chen, L.; Yang, J.; Dai, L.; et al. In situ growth, structure characterization, and enhanced photocatalysis of high-quality, single-crystalline ZnTe/ZnO branched nanoheterostructures. *Nanoscale* **2011**, *3*, 4418−4426.

(67) Zhang, J.; Jin, S.; Fry, H. C.; Peng, S.; Shevchenko, E.; Wiederrecht, G. P.; Rajh, T. Synthesis and characterization of wurtzite ZnTe nanorods with controllable aspect ratios. *J. Am. Chem. Soc.* **2011**, *133*, 15324−15327.

(68) Mayengbam, R.; Tripathy, S.; Palai, G.; Dhar, S. First-principles study of phase transition, electronic, elastic and optical properties of defect chalcopyrite ZnGa2Te4 semiconductor under different pressures. *J. Phys. Chem. Solids* **2018**, *119*, 193−201.

(69) Shi, C.; Chan, K.; Yoo, J. S.; Nørskov, J. K. Barriers of Electrochemical CO2 Reduction on Transition Metals. *Org. Process Res. Dev.* **2016**, *20*, 1424−1430.

(70) Föhlisch, A.; Nyberg, M.; Bennich, P.; Triguero, L.; Hasselström, J.; Karis, O.; Pettersson, L. G. M.; Nilsson, A. The bonding of CO to metal surfaces. *J. Chem. Phys.* **2000**, *112*, 1946−1958.

(71) Hu, P.; King, D.; Lee, M.-H.; Payne, M. Orbital mixing in CO chemisorption on transition metal surfaces. *Chem. Phys. Lett.* **1995**, *246*, 73−78.

(72) Michalsky, R.; Zhang, Y.-J.; Medford, A. J.; Peterson, A. A. Departures from the Adsorption Energy Scaling Relations for Metal Carbide Catalysts. *J. Phys. Chem. C* **2014**, *118*, 13026−13034.

(73) Calle-Vallejo, F.; Martínez, J. I.; García-Lastra, J. M.; Sautet, P.; Loffreda, D. Fast Prediction of Adsorption Properties for Platinum Nanocatalysts with Generalized Coordination Numbers. *Angew. Chem., Int. Ed.* **2014**, *53*, 8316−8319.

(74) Peterson, A. A.; Grabow, L. C.; Brennan, T. P.; Shong, B.; Ooi, C.; Wu, D. M.; Li, C. W.; Kushwaha, A.; Medford, A. J.; Mbuga, F.; et al. Finite-Size Effects in O and CO Adsorption for the Late Transition Metals. *Top. Catal.* **2012**, *55*, 1276−1282.

(75) Billeter, E.; Terreni, J.; Borgschulte, A. Hydride Formation Diminishes CO 2 Reduction Rate on Palladium. *ChemPhysChem* **2019**, *20*, 1398−1403.